Parameterization of the Radiative Properties of Cirrus Clouds

QIANG FU AND K. N. LIOU

Department of Meteorology/CARSS, University of Utah, Salt Lake City, Utah

(Manuscript received 6 July 1992, in final form 7 October 1992)

ABSTRACT

A new approach for parameterization of the broadband solar and infrared radiative properties of ice clouds has been developed. This parameterization scheme integrates in a coherent manner the δ-four-stream approximation for radiative transfer, the correlated k-distribution method for nongray gaseous absorption, and the scattering and absorption properties of hexagonal ice crystals. A mean effective size is used, representing an area-weighted mean crystal width, to account for the ice crystal size distribution with respect to radiative calculations. Based on physical principles, the basic single-scattering properties of ice crystals, including the extinction coefficient divided by ice water content, single-scattering albedo, and expansion coefficients of the phase function, can be parameterized using third-degree polynomials in terms of the mean effective size. In the development of this parameterization the results computed from a light scattering program that includes a geometric ray-tracing program for size parameters larger than 30 and the exact spheroid solution for size parameters less than 30 are used. The computations are carried out for 11 observed ice crystal size distributions and cover the entire solar and thermal infrared spectra. Parameterization of the single-scattering properties is shown to provide an accuracy within about 1%. Comparisons have been carried out between results computed from the model and those obtained during the 1986 cirrus FIRE IFO. It is shown that the model results can be used to reasonably interpret the observed IR emissivities and solar albedo involving cirrus clouds. The newly developed scheme has been employed to investigate the radiative effects of ice crystal size distributions. For a given ice water path, cirrus clouds with smaller mean effective sizes reflect more solar radiation, trap more infrared radiation, and produce stronger cloud-top cooling and cloud-base heating. The latter effect would enhance the in-cloud heating rate gradients. Further, the effects of ice crystal size distribution in the context of IR greenhouse versus solar albedo effects involving cirrus clouds are presented with the aid of the upward flux at the top of the atmosphere. In most cirrus cases, the IR greenhouse effect outweighs the solar albedo effect. One exception occurs when a significant number of small ice crystals are present. The present scheme for radiative transfer in the atmosphere involving cirrus clouds is well suited for incorporation in numerical models to study the climatic effects of cirrus clouds, as well as to investigate interactions and feedbacks between cloud microphysics and radiation.

1. Introduction

Cirrus clouds are globally distributed, being present at all latitudes and without respect to land or sea or season of the year. They regularly cover about 20%–30% of the globe and strongly influence weather and climate processes through their effects on the radiation budget of the earth and the atmosphere (Liou 1986). The importance of cirrus clouds in weather and climate research can be recognized by the intensive field observations that have been conducted as a major component of the First ISCCP Regional Experiment in October–November 1986 (Starr 1987) and more recently in November–December 1991.

Cirrus clouds possess a number of unique features. In addition to being global and located high in the troposphere and extending to the lower stratosphere on some occasions, they contain almost exclusively nonspherical ice crystals of various shapes, such as bullet rosettes, plates, and columns. There are significant computational and observational difficulties in determining the radiative properties of cirrus clouds. A reliable and efficient determination of the radiative properties of cirrus clouds requires the fundamental scattering and absorption data involving nonspherical ice crystals. In addition, appropriate incorporation of gaseous absorption in scattering cloudy atmospheres and an efficient radiative transfer methodology are also required.

Although parameterization of the broadband radiative properties for cirrus clouds has been presented by Liou and Wittman (1979) in terms of ice water content, such parameterization used the scattering and absorption properties of circular cylinders without accounting for the effects of the hexagonal structure of ice crystals. Moreover, the effects of ice crystal size distribution were not included in the parameterization. Using area-equivalent or volume-equivalent ice spheres to approximate hexagonal ice crystals for scattering and absorption properties has been shown to be inadequate,

Corresponding author address: Professor K. N. Liou, Department of Meteorology, University of Utah, 809 William C. Browning Building, Salt Lake City, UT 84112.

and frequently misleading. This is evident in interpreting the scattering and polarization patterns from ice clouds (Takano and Liou 1989) and the observed radiative properties of cirrus clouds, in particular, the cloud albedo (Stackhouse and Stephens 1991).

In this paper, we wish to develop a new approach for the parameterization of the broadband solar and infrared radiative properties of ice crystal clouds. Three major components are integrated in this parameterization, including the scattering and absorption properties of hexagonal ice crystals, the δ-four-stream approximation for radiative transfer, and the correlated k-distribution method for nongray gaseous absorption. Compared with more sophisticated models and aircraft observations, the present parameterization has been shown to be accurate and efficient for flux and heating rate calculations. In section 2, we present parameterization of the single-scattering properties of ice crystals. The manner in which the radiative flux transfer is parameterized using the δ-four-stream approximation and the correlated k-distribution is discussed in section 3. Section 4 presents some comparisons between theoretical results and observed data involving cloud emissivity and albedo. In section 5, we present the effect of ice crystal size distribution on cloud heating rates and on the question of cloud radiative forcing. Summary and conclusions are given in section 6.

2. Parameterization of the single-scattering properties of ice crystals

a. Physical bases

The calculations of the single-scattering properties, including the phase function, single-scattering albedo, and extinction coefficient, require a light scattering program and the detailed particle size distribution. The calculations are usually time consuming. If radiation calculations are to interact with an evolving cloud where particle size distribution varies as a function of time and/or space, the computer time needed for examining just this aspect of the radiation program would be formidable, even with a supercomputer. Thus, there is a practical need to simplify the computational procedure for the calculation of the single-scattering properties of cloud particles. Since spheres scatter an amount of light proportionate to their cross-section area, a mean effective radius, which is defined as the mean radius that is weighted by the cross-section area of spheres, has been used in conjunction with radiation calculations (Hansen and Travis 1974). Higher-order definition, such as dispersion of the droplet size, may be required in order to more accurately represent the droplet size distribution.

Ice crystals are nonspherical and ice crystal size distributions are usually expressed in terms of the maximum dimension (or length). Representation of the size distribution for ice crystals is much more involved than that for water droplets. To the extent that scattering of light is proportional to the cross-section area of nonspherical particles, we may use a mean effective size analogous to the mean effective radius defined for spherical water droplets as follows:

$$D_e = \int_{L_{\min}}^{L_{\max}} D \cdot DLn(L)dL \Big/ \int_{L_{\min}}^{L_{\max}} DLn(L)dL, \tag{2.1}$$

where D is the width of an ice crystal, $n(L)$ denotes the ice crystal size distribution, and $L_{\min}$ and $L_{\max}$ are the minimum and maximum lengths of ice crystals, respectively. A similar definition for circular cylinders has also been proposed by Platt and Harshvardhan (1988). Based on aircraft observations by Ono (1969) and Auer and Veal (1970), the width may be related to the length L. It follows that the mean effective width (or size) can be defined solely in terms of ice crystal size distribution. The geometric cross section area for oriented hexagonal ice crystals generally deviates from DL [see Eq. (2.4) for the condition of random orientation]. To the extent that D is related to L, the definition of D_e in Eq. (2.1), which is an approach to represent ice crystal size distribution, should be applicable to ice crystals with hexagonal structure. The numerator in Eq. (2.1) is related to the ice water content (IWC) in the form

$$\text{IWC} = \frac{3\sqrt{3}}{8} \rho_i \int_{L_{\min}}^{L_{\max}} D \cdot DLn(L)dL, \tag{2.2}$$

where the volume of a hexagonal ice crystal, $3\sqrt{3}D^2L/8$, is used and ρ_i is the density of ice. We shall confine our study to the use of the mean effective size to represent ice crystal size distribution in the single-scattering calculation for ice crystals.

The extinction coefficient is defined by

$$\beta = \int_{L_{\min}}^{L_{\max}} \sigma(D, L)n(L)dL, \tag{2.3}$$

where σ is the extinction cross section for a single crystal. In the limits of geometric optics and using hexagonal ice crystals that are randomly oriented in space, the extinction cross section may be expressed by (Takano and Liou 1989)

$$\sigma = \frac{3}{2} D\left(\frac{\sqrt{3}}{4} D + L\right). \tag{2.4}$$

Substituting Eq. (2.4) into Eq. (2.3) and using the definitions of D_e and IWC, we have

$$\beta = \text{IWC}\left(\frac{1}{\rho_i} \int_{L_{\min}}^{L_{\max}} D^2 n(L)dL \Big/ \int_{L_{\min}}^{L_{\max}} D^2 Ln(L)dL + \frac{4}{\sqrt{3}\rho_i} \frac{1}{D_e}\right). \tag{2.5a}$$

The first term on the right cannot be defined in terms

of D_e directly. Since $D < L$, however, this term should be much smaller than the second term, which also involves a factor $4/\sqrt{3}$. To the extent that D is related to L, the first term may be approximated by $a + b'/D_e$, where $b' \ll 4/\sqrt{3}\rho_i$ and a is a certain constant. Using this argument, we obtain the following relationship:

$$\beta \approx \text{IWC}(a + b/D_e), \tag{2.5b}$$

where $b = b' + 4/\sqrt{3}\rho_i$. Using the observed ice crystal size distributions described below, we also show that β/IWC and $1/D_e$ are linearly related in the solar spectral region. Based on the preceding analysis, it is clear that the extinction coefficient is a function of both IWC and mean effective size.

Because cloud absorption is critically dependent on the variation of the single-scattering albedo, it must be accurately parameterized. For a given ice crystal size distribution, the single-scattering albedo, $\tilde{\omega}$, is defined by

$$1 - \tilde{\omega} = \int_{L_{\min}}^{L_{\max}} \sigma_a n(L) dL \Big/ \int_{L_{\min}}^{L_{\max}} \sigma n(L) dL, \tag{2.6}$$

where σ_a denotes the absorption cross section for a single crystal. When absorption is small, σ_a is approximately equal to the product of the imaginary part of the refractive index of ice, m_i, and the particle volume; namely,

$$\sigma_a = \frac{3\sqrt{3}\pi m_i(\lambda)}{2\lambda} D^2 L, \tag{2.7}$$

where λ is the wavelength. Using the extinction and absorption cross sections defined in Eqs. (2.4) and (2.7) and noting that D is related to L, based on observations, we obtain

$$1 - \tilde{\omega} \approx c + dD_e, \tag{2.8}$$

where c and d are certain coefficients.

In the preceding discussion, we have used the geometric optics limit to derive the expressions for the extinction coefficient and single-scattering albedo. In view of the observed ice crystal sizes in cirrus clouds ($\sim$20–2000 μm), the simple linear relationships denoted in Eqs. (2.5b) and (2.8) should be valid for solar wavelengths (0.2–4 μm). For thermal infrared wavelengths (e.g., 10 μm), the geometric optics approximation may not be appropriate for small ice crystals. We note from aircraft observations, however, that there is a good linear relationship between the extinction coefficient in the infrared spectrum and the extinction coefficient derived based upon the large-particle approximation (Foot 1988).

b. *A generalized parameterization*

The linear relationship between β/IWC and $1/D_e$ shown in Eq. (2.5b) is derived based on the geometric optics approximation and the assumption that ice crystals are randomly oriented in space. The linear relationship between $\tilde{\omega}$ and D_e shown in Eq. (2.8) is based on the assumption that ice crystal absorption is small and that ice crystals are randomly oriented. For general cases, we would expect that higher-order expansions may be needed to define more precisely the single-scattering properties of ice crystals in terms of the mean effective size. Thus, we postulate that

$$\beta = \text{IWC} \sum_{n=0}^{N} a_n / D_e^n, \tag{2.9}$$

$$1 - \tilde{\omega} = \sum_{n=0}^{N} b_n D_e^n, \tag{2.10}$$

where a_n and b_n are certain coefficients, which must be determined from numerical fitting, and N is the total number of terms required to achieve a prescribed accuracy. When $N = 1$, Eqs. (2.9) and (2.10) are exactly the same as Eqs. (2.5b) and (2.8). When $N = 2$, the term $1/D_e^2$ is proportional to the variance of ice crystal size distribution. Based on numerical experimentation described in subsection c, we find $N = 2$ is sufficient for the extinction coefficient expression to achieve an accuracy within 1%. For the single-scattering albedo, we find that $N = 3$ is required.

For nonspherical particles randomly oriented in space, the phase function is a function of the scattering angle, θ. The phase function is usually expanded in a series of Legendre polynomials P_l in radiative transfer calculations in the form

$$P(\cos\theta) = \sum_{l=0}^{M} \tilde{\omega}_l P_l(\cos\theta), \tag{2.11}$$

where we set $\tilde{\omega}_0 = 1$. Since the phase function is dependent on ice crystal size distribution, the expansion coefficients must also be related to ice crystal size distribution, which is represented by the mean effective size in the present study. In the case of hexagonal ice crystals, in addition to the diffraction, scattered energy is also produced by the δ-function transmission through parallel planes at $\theta = 0$ (Takano and Liou 1989). Using the similarity principle for radiative transfer, the expansion coefficients in the context of the four-stream approximation can be expressed by

$$\tilde{\omega}_l = (1 - f_\delta)\tilde{\omega}_l^* + f_\delta(2l + 1), \quad l = 1, 2, 3, 4, \tag{2.12}$$

where $\tilde{\omega}_l^*$ represents the expansion coefficients for the phase function in which the forward δ-function peak has been removed, and f_δ is the contribution from the forward δ-function peak. In our notation, $\tilde{\omega}_1 = 3g$, where g is the asymmetry factor. The δ-function peak contribution has been evaluated by Takano and Liou and is a function of ice crystal size. The f_δ value increases with increasing L/D value due to a greater probability for plane-parallel transmission. We may

express $\tilde{\omega}_l^*$ and f_δ in terms of the mean effective size as follows:

$$\tilde{\omega}_l^* = \sum_{n=0}^{N} c_{n,l} D_e^n, \tag{2.13a}$$

$$f_\delta = \sum_{n=0}^{N} d_n D_e^n, \tag{2.13b}$$

where $c_{n,l}$ and d_n are certain coefficients. Based on numerical experimentation described in subsection *c*, we find $N = 3$ is sufficient to achieve an accuracy within 1%.

In the thermal infrared wavelengths, halo and δ-transmission peak features in the phase function are largely suppressed due to strong absorption. For this reason and to a good approximation, we may use the asymmetry factor to represent the phase function via the Henyey–Greenstein function in the form

$$\tilde{\omega}_l = (2l + 1)g^l. \tag{2.14}$$

The asymmetry factor may also be expressed in terms of the effective mean size as follows:

$$g(\mathrm{IR}) = \sum_{n=0}^{N} c'_n D_e^n, \tag{2.15}$$

where c'_n again is a certain coefficient and $N = 3$ is sufficient in the expansion.

c. *Determination of the coefficients in the parameterization*

The coefficients in Eqs. (2.9), (2.10), (2.13), and (2.15) are determined from numerical fitting to the data computed from "exact" light scattering and absorption programs that include the following. For size parameters larger than about 30, we use the results computed from a geometric ray-tracing program for hexagonal ice crystals developed by Takano and Liou (1989). Note that the parameterization coefficients may be updated if the results for other types of ice crystals, such as bullet rosettes and hollow columns, are available. For size parameters less than about 30, the laws of geometric optics are generally not applicable. Since the exact solution for hexagonal ice crystals based on either the wave equation approach or other integral methods for size parameters on the order of 20–30 has not been developed, we use the results computed from a light scattering program for spheroids developed by Asano and Sato (1980). We have tested and modified this program (Takano et al. 1992) and found that it can be applied to size parameters less than about 30. Naturally occurring ice crystals will have a hexagonal structure that cannot be approximated by spheroids. However, small size parameters are usually associated with infrared wavelengths, where ice is highly absorbing. It is likely that the detailed shape factor may not be critical in scattering and absorption calculations. Further inquiry into this problem appears necessary.

In the present "exact" computations, 11 ice crystal size distributions from in situ aircraft observations were employed. Table 1 shows the number densities, IWCs, and mean effective sizes for these 11 size distributions. The first two types are for the cirrostratus (Cs) and cirrus uncinus presented by Heymsfield (1975), while the next two types are modified distributions given by Heymsfield and Platt (1984) corresponding to warm and cold cirrus clouds. The size distributions of cirrus clouds at temperatures of −20°, −40°, and −60°C were obtained from the parameterization results presented by Heymsfield and Platt (1984). Other cirrus types, Ci (22 October, 25 October, 1 November, and 2 November), were the ice crystal size distributions derived from the 1986 FIRE cirrus experiments (A. Heymsfield, personal communication). The 11 size distributions cover a reasonable range of cloud microphysical properties in terms of IWC (6.6×10^{-4}–0.11 g m^{-3}) and mean effective size (23.9–123.6 μm) as shown in Table 1. For scattering and absorption calculations, these size distributions have been discretized in five regions. The aspect ratios, L/D, used are 20/20, 50/40, 120/60, 300/100, and 750/160 (in units of μm/μm), roughly corresponding to the observations reported by Ono (1969) and Auer and Veal (1970).

In the single-scattering calculations, the refractive indices for ice, compiled by Warren (1984), were used. In order to resolve the variation in the refractive index of ice and account for the gaseous absorption, 6 and 12 bands were selected for solar and thermal IR regions, respectively. The spectral division is shown in Table 2, where the index for the spectral band ($i = 1, 2, \cdots, 18$) is defined. The complex indices of refraction at each wavelength are averaged values over the spectral band, weighted by the solar irradiance (Thekaekara 1973) in solar spectrum and by the Planck function ($T = -40$°C) in thermal IR spectrum. This temperature is a typical value for cirrus clouds. The single-scattering calculations were carried out at the central

TABLE 1. Characteristics of the 11 ice crystal size distributions employed in the present study.

Particle size distribution	Number of particles (cm^{-3})	Ice water content (g m^{-3})	Mean effective size (μm)
Cs	0.187	4.765×10^{-3}	41.5
Ci Uncinus	0.213	1.116×10^{-1}	123.6
Ci (cold)	0.176	1.110×10^{-3}	23.9
Ci (warm)	0.442	9.240×10^{-3}	47.6
Ci ($T = -20$°C)	0.247	8.613×10^{-3}	57.9
Ci ($T = -40$°C)	0.187	9.177×10^{-3}	64.1
Ci ($T = -60$°C)	0.065	6.598×10^{-4}	30.4
Ci (22 Oct)	0.052	1.609×10^{-2}	104.1
Ci (25 Oct)	0.072	2.923×10^{-2}	110.4
Ci (1 Nov)	0.032	4.968×10^{-3}	75.1
Ci (2 Nov)	0.038	1.406×10^{-2}	93.0

TABLE 2. Spectral division used in the parameterization.

Solar spectrum			Infrared spectrum		
Band i	Central λ (μm)	Band limits (μm)	Band i	Central λ (μm)	Band limits (cm^{-1})
1	0.55	0.2–0.7	7	4.9	2200–1900
2	1.0	0.7–1.3	8	5.6	1900–1700
3	1.6	1.3–1.9	9	6.5	1700–1400
4	2.2	1.9–2.5	10	7.6	1400–1250
5	3.0	2.5–3.5	11	8.5	1250–1100
6	3.7	3.5–4.0	12	9.6	1100–980
			13	11.3	980–800
			14	13.7	800–670
			15	16.6	670–540
			16	21.5	540–400
			17	30.0	400–280
			18	70.0	280–1

wavelength for each spectral band. The coefficients in Eqs. (2.9), (2.10), (2.13), and (2.15) determined by numerical fitting using the "exact" results are listed in Tables 3–5. In the solar spectrum where the law of geometric optics is valid, the extinction coefficients β for a given size distribution are the same regardless of the wavelength, as shown in Table 3. The optical depth $\tau = \beta\Delta z$ can be obtained if the cloud thickness Δz is given. Figures 1–2 show the fitting for β/IWC, $\tilde{\omega}$, and g in the spectral intervals 1.9–2.5 μm and 800–980 cm^{-1}, respectively. For the solar spectrum, we use band number four (1.9–2.5 μm) as an example, because the single-scattering properties in this band significantly depend on size distribution. The linear relationship between β/IWC and $1/D_e$ postulated in Eq. (2.5b) is clearly shown in Fig. 1a. This linear relationship is valid for all other solar bands, because the extinction cross sections for solar bands in the limit of the geometric optics approach are the same, as pointed out previously. The nonlinearity between $\tilde{\omega}$ and D_e becomes important for small $\tilde{\omega}$. This is because the linear relationship developed in Eq. (2.8) is based on the weak absorption assumption. The band 800–980 cm^{-1} is located in the atmospheric window, where the greenhouse effect of clouds is most pronounced. It can be seen that very good fits for single-scattering properties in both solar and infrared spectra are obtained. The relative errors are less than ~1%. Other spectral bands also show similar accuracies.

It is known that the minimum ice crystal length that the present optical probe can measure is about 20 μm. To investigate the potential effects of small ice crystals that may exist in cirrus clouds on parameterizations of the single-scattering properties, we used the 11 observed ice crystal size distributions and extrapolated these distributions from 20 to 10 μm in the logarithmic scale. The resulting mean effective sizes range from 18.9 to 122.7 μm. Using these sizes, the numerical fitting coefficients vary only slightly and do not affect the accuracy of the preceding parameterized single-scattering properties. In the present study, ice crystals are assumed to be randomly oriented in space. In cases when cirrus clouds contain horizontally oriented ice crystals, parameterizations would require modifications. The extinction coefficient, single-scattering albedo, and phase function would depend on the incident direction. The radiative transfer scheme would also require adjustments to account for anisotropic properties. Since fluxes are involved in the parameterization, we anticipate that the modifications should not significantly affect the results and conclusions derived from this study. At any rate, this is an area requiring further research efforts.

3. Parameterization of radiative flux transfer

a. Radiative transfer scheme

We follow the δ-four-stream model developed by Liou et al. (1988) for the calculations of solar radiative flux transfer in a single homogeneous layer. The solution, like various two-stream methods, is in analytic form so that the computational effort involved is minimal. As demonstrated in that paper, results from the δ-four-stream approximation can yield relative accuracies within ~5%.

To obtain a single treatment of solar and infrared radiation, we extend the δ-four-stream approach to the transfer of infrared radiation, in which the optical depth dependence of the Planck function must be known. The Planck function can be approximately expressed in terms of the optical depth in the form

$$B(\tau) = B_0 \exp(\tau/\tau_1 \ln B_1/B_0), \qquad (3.1)$$

where τ_1 is the optical depth of a layer, and B_0 and B_1 are the Planck functions corresponding to the temperature at the top and bottom of this layer, respectively. This exponential approximation for the Planck func-

TABLE 3. Values of empirical coefficients in Eq. (2.9) for the parameterization of the extinction coefficient β (m^{-1}). Note that the coefficients are determined by using an ice density ρ_i of 0.9167 g cm^{-3}. For other ice densities ρ_i^*, they should be adjusted by a factor ρ_i/ρ_i^*. (The units for D_e and IWC are in μm and g m^{-3}, respectively.)

Band i	a_0	a_1	a_2
1–6	-6.656×10^{-3}	3.686	0.0
7	-7.770×10^{-3}	3.734	11.85
8	-8.088×10^{-3}	3.717	17.17
9	-8.441×10^{-3}	3.715	19.48
10	-9.061×10^{-3}	3.741	26.48
11	-9.609×10^{-3}	3.768	34.11
12	-1.153×10^{-2}	4.109	17.32
13	-8.294×10^{-3}	3.925	1.315
14	-1.026×10^{-2}	4.105	16.36
15	-1.151×10^{-2}	4.182	31.13
16	-1.704×10^{-2}	4.830	16.27
17	-1.741×10^{-2}	5.541	−58.42
18	-7.752×10^{-3}	4.624	−42.01

TABLE 4. Values of empirical coefficients in Eq. (2.10) for the parameterization of the single-scattering albedo $\tilde{\omega}$. (The units for D_e are in μm.)

Band i	b_0	b_1	b_2	b_3
1	$.10998 \times 10^{-5}$	$-.26101 \times 10^{-7}$	$.10896 \times 10^{-8}$	$-.47387 \times 10^{-11}$
2	$.20208 \times 10^{-4}$	$.96483 \times 10^{-5}$	$.83009 \times 10^{-7}$	$-.32217 \times 10^{-9}$
3	$.13590 \times 10^{-3}$	$.73453 \times 10^{-3}$	$.28281 \times 10^{-5}$	$-.18272 \times 10^{-7}$
4	$-.16598 \times 10^{-2}$	$.20933 \times 10^{-2}$	$-.13977 \times 10^{-5}$	$-.18703 \times 10^{-7}$
5	.46180	$.24471 \times 10^{-3}$	$-.27839 \times 10^{-5}$	$.10379 \times 10^{-7}$
6	$.42362 \times 10^{-1}$	$.86425 \times 10^{-2}$	$-.75519 \times 10^{-4}$	$.24056 \times 10^{-6}$
7	.19960	$.37800 \times 10^{-2}$	$-.14910 \times 10^{-4}$	.0
8	.30140	$.26390 \times 10^{-2}$	$-.11160 \times 10^{-4}$	.0
9	.39080	$.12720 \times 10^{-2}$	$-.55640 \times 10^{-5}$	.0
10	.31050	$.26030 \times 10^{-2}$	$-.11390 \times 10^{-4}$	.0
11	.20370	$.42470 \times 10^{-2}$	$-.18100 \times 10^{-4}$	.0
12	.23070	$.38300 \times 10^{-2}$	$-.16160 \times 10^{-4}$	.0
13	.56310	$-.14340 \times 10^{-2}$	$.62980 \times 10^{-5}$	.0
14	.52070	$-.97780 \times 10^{-3}$	$.37250 \times 10^{-5}$	.0
15	.32540	$.34340 \times 10^{-2}$	$-.30810 \times 10^{-4}$	$.91430 \times 10^{-7}$
16	.10280	$.50190 \times 10^{-2}$	$-.20240 \times 10^{-4}$	.0
17	.39640	$-.31550 \times 10^{-2}$	$.64170 \times 10^{-4}$	$-.29790 \times 10^{-6}$
18	.80790	$-.70040 \times 10^{-2}$	$.52090 \times 10^{-4}$	$-.14250 \times 10^{-6}$

TABLE 5a. Values of empirical coefficients in Eq. (2.13) for parameterization of the expansion coefficients for the phase function in the solar wavelengths. (The units for D_e are in μm.)

Band i	l	$c_{0,l}$	$c_{1,l}$	$c_{2,l}$	$c_{3,l}$
1	1	$.22110 \times 10^{1}$	$-.10398 \times 10^{-2}$	$.65199 \times 10^{-4}$	$-.34498 \times 10^{-6}$
	2	$.32201 \times 10^{1}$	$.94227 \times 10^{-3}$	$.80947 \times 10^{-4}$	$-.47428 \times 10^{-6}$
	3	$.41610 \times 10^{1}$	$.74396 \times 10^{-3}$	$.82690 \times 10^{-4}$	$-.45251 \times 10^{-6}$
	4	$.51379 \times 10^{1}$	$.51545 \times 10^{-2}$	$.11881 \times 10^{-4}$	$-.15556 \times 10^{-6}$
2	1	$.22151 \times 10^{1}$	$-.77982 \times 10^{-3}$	$.63750 \times 10^{-4}$	$-.34466 \times 10^{-6}$
	2	$.31727 \times 10^{1}$	$.15597 \times 10^{-2}$	$.82021 \times 10^{-4}$	$-.49665 \times 10^{-6}$
	3	$.40672 \times 10^{1}$	$.25800 \times 10^{-2}$	$.71550 \times 10^{-4}$	$-.43051 \times 10^{-6}$
	4	$.49882 \times 10^{1}$	$.86489 \times 10^{-2}$	$-.18318 \times 10^{-4}$	$-.59275 \times 10^{-7}$
3	1	$.22376 \times 10^{1}$	$.10293 \times 10^{-2}$	$.50842 \times 10^{-4}$	$-.30135 \times 10^{-6}$
	2	$.31549 \times 10^{1}$	$.47115 \times 10^{-2}$	$.70684 \times 10^{-4}$	$-.47622 \times 10^{-6}$
	3	$.39917 \times 10^{1}$	$.82830 \times 10^{-2}$	$.53927 \times 10^{-4}$	$-.41778 \times 10^{-6}$
	4	$.48496 \times 10^{1}$	$.15998 \times 10^{-1}$	$-.39320 \times 10^{-4}$	$-.43862 \times 10^{-7}$
4	1	$.23012 \times 10^{1}$	$.33854 \times 10^{-2}$	$.23528 \times 10^{-4}$	$-.20068 \times 10^{-6}$
	2	$.31730 \times 10^{1}$	$.93439 \times 10^{-2}$	$.36367 \times 10^{-4}$	$-.38390 \times 10^{-6}$
	3	$.39298 \times 10^{1}$	$.16424 \times 10^{-1}$	$.10502 \times 10^{-4}$	$-.35086 \times 10^{-6}$
	4	$.47226 \times 10^{1}$	$.25872 \times 10^{-1}$	$-.77542 \times 10^{-4}$	$-.21999 \times 10^{-7}$
5	1	$.27975 \times 10^{1}$	$.29741 \times 10^{-2}$	$-.32344 \times 10^{-4}$	$.11636 \times 10^{-6}$
	2	$.43532 \times 10^{1}$	$.11234 \times 10^{-1}$	$-.12081 \times 10^{-3}$	$.43435 \times 10^{-6}$
	3	$.56835 \times 10^{1}$	$.24681 \times 10^{-1}$	$-.26480 \times 10^{-3}$	$.95314 \times 10^{-6}$
	4	$.68271 \times 10^{1}$	$.42788 \times 10^{-1}$	$-.45615 \times 10^{-3}$	$.16368 \times 10^{-5}$
6	1	$.19655 \times 10^{1}$	$.20094 \times 10^{-1}$	$-.17067 \times 10^{-3}$	$.50806 \times 10^{-6}$
	2	$.28803 \times 10^{1}$	$.36091 \times 10^{-1}$	$-.28365 \times 10^{-3}$	$.79656 \times 10^{-6}$
	3	$.34613 \times 10^{1}$	$.58525 \times 10^{-1}$	$-.46455 \times 10^{-3}$	$.13444 \times 10^{-5}$
	4	$.39568 \times 10^{1}$	$.81480 \times 10^{-1}$	$-.64777 \times 10^{-3}$	$.19022 \times 10^{-5}$
		d_0	d_1	d_2	d_3
1		.12495	$-.43582 \times 10^{-3}$	$.14092 \times 10^{-4}$	$-.69565 \times 10^{-7}$
2		.12363	$-.44419 \times 10^{-3}$	$.14038 \times 10^{-4}$	$-.68851 \times 10^{-7}$
3		.12117	$-.48474 \times 10^{-3}$	$.12495 \times 10^{-4}$	$-.62411 \times 10^{-7}$
4		.11581	$-.55031 \times 10^{-3}$	$.98776 \times 10^{-5}$	$-.50193 \times 10^{-7}$
5		$-.15968 \times 10^{-3}$	$.10115 \times 10^{-4}$	$-.12472 \times 10^{-6}$	$.48667 \times 10^{-9}$
6		.13830	$-.18921 \times 10^{-2}$	$.12030 \times 10^{-4}$	$-.31698 \times 10^{-7}$

TABLE 5b. Values of empirical coefficients in Eq. (2.15) for parameterization of the asymmetry factor in the infrared wavelengths. (The units for D_e are in μm.)

Band i	c_0'	c_1'	c_2'	c_3'
7	.79550	2.524×10^{-3}	-1.022×10^{-5}	0.0
8	.86010	1.599×10^{-3}	-6.465×10^{-6}	0.0
9	.89150	1.060×10^{-3}	-4.171×10^{-6}	0.0
10	.87650	1.198×10^{-3}	-4.485×10^{-6}	0.0
11	.88150	9.858×10^{-4}	-3.116×10^{-6}	0.0
12	.91670	5.499×10^{-4}	-1.507×10^{-6}	0.0
13	.90920	9.295×10^{-4}	-3.877×10^{-6}	0.0
14	.84540	1.429×10^{-3}	-5.859×10^{-6}	0.0
15	.76780	2.571×10^{-3}	-1.041×10^{-5}	0.0
16	.72900	2.132×10^{-3}	-5.584×10^{-6}	0.0
17	.70240	4.581×10^{-3}	-3.054×10^{-5}	6.684×10^{-8}
18	.22920	1.724×10^{-2}	-1.573×10^{-4}	4.995×10^{-7}

tion in optical depth has an accuracy similar to the linear approximation for the Planck function developed by Wiscombe (1976). Since the direct solar radiation source has an exponential function form in terms of optical depth, the formulation of the δ-four-stream approximation for infrared wavelengths is the same as that for solar wavelengths. For this reason, the computer program is simplified and the computational speed is enhanced.

In the limit of pure molecular absorption at infrared wavelengths, τ_1 may approach zero for some bands. The major advantage of using Eq. (3.1) is that the solution of the transfer equation is numerically stable when $\tau_1 \to 0$. If the linear approximation in τ is used, the roundoff error may lead to an unstable solution when τ_1 is very small. We note that the higher-order polynomial approximation in τ for the Planck function can also lead to an unstable solution. As in the case of solar wavelengths, we perform relative accuracy checks for infrared wavelengths with respect to "exact" results computed from the adding method for radiative transfer (Liou 1992). Numerical results reveal that the errors in the δ-four-stream scheme in computing IR cloud emissivity are typically less than 1%. Systematic equations for this scheme that are required in numerical calculations are given in the Appendix.

For applications of the δ-four-stream scheme to nonhomogeneous atmospheres, the atmosphere is divided into N homogeneous layers with respect to the single-scattering albedo and phase function. The $4 \times N$ unknown coefficients in the analytic solution for the transfer equation are determined following the procedure described in Liou (1975). A numerically stable program has been developed to solve the system of linear equations by utilizing the property that the coefficient matrix is a sparse matrix. While this method is similar to the Gaussian elimination method with back substitution, it is carefully optimized so as to minimize the mathematical operations. We perform partial pivoting (interchanging rows only) to guarantee that a solution always exists. In order to avoid a fatal overflow problem, we follow the scaling technique developed by Stamnes and Conklin (1984) so that numerical solutions can be carried out for large optical depths. Numerical problems that may occur when the single-scattering albedo $\tilde{\omega} = 0$ or 1 are also resolved in the present

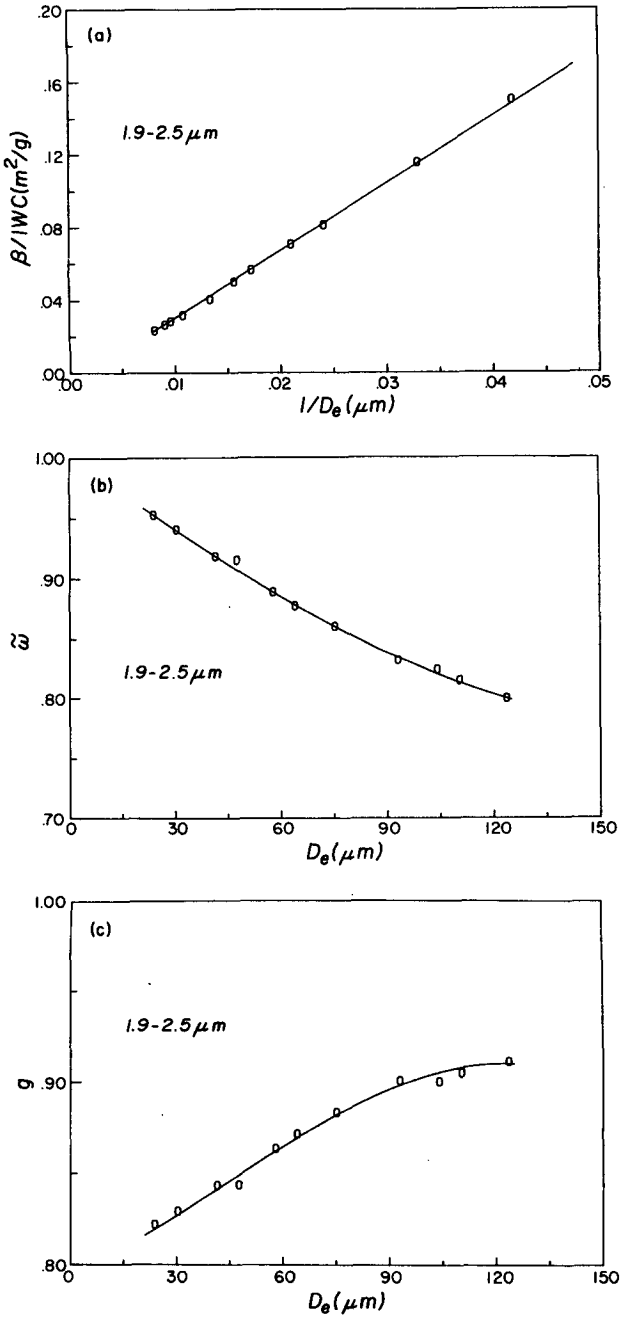

FIG. 1. (a) Extinction coefficient/IWC, (b) single-scattering albedo, and (c) asymmetry factor as functions of the mean effective size for the spectral interval 1.9–2.5 μm. The "0" points represent exact results from the light scattering program, and the curves are from the parameterizations.

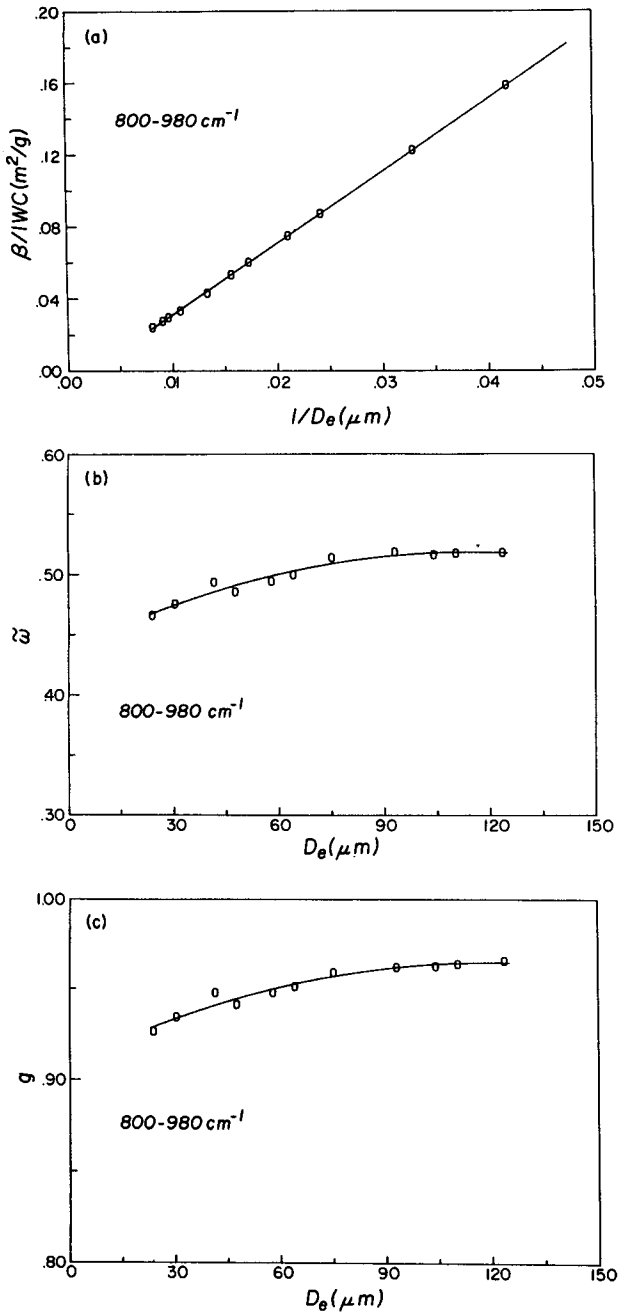

FIG. 2. Same as in Fig. 1 except for the spectral interval 800–980 cm^{-1}.

program. Using results from the adding method as a reference, errors in the δ-four-stream scheme for the nonhomogeneous multilayer cases remain within ~5%. Transfer of infrared radiation has not been treated satisfactorily by the two-stream techniques, because they do not produce reliable results in the limit of no scattering. This problem is circumvented in the present algorithm by using the "double Gauss" quadrature (Sykes 1951), which produces a correct relation between the flux and intensity from an isotropic source.

Using the δ-four-stream scheme along with the parameterized single-scattering properties reported in section 2, we calculate the solar reflectance and transmittance properties for typical ice clouds with different thicknesses and solar zenith angles. These properties are defined by $r = \sum_i r_i w_i$ and $t = \sum_i t_i w_i$ where r_i and t_i denote the reflectance and transmittance (direct plus diffuse) for an individual band, and w_i is the fraction of solar flux in the band. The relative errors are examined with respect to the "exact" results computed from the adding method using the "exact" phase function. Using Ci (1 November) as an example, Figs. 3a and 3b show the "exact" reflectance and transmittance, respectively, and Figs. 3c and 3d show the corresponding percentage errors in the δ-four-stream scheme for reflectance and transmittance. The δ-four-stream results in most cases achieve relative accuracies within ~5%. The errors shown in Figs. 3c and 3d contain not only errors due to the δ-four-stream approximation, but also errors produced by the parameterized single-scattering properties for ice clouds. Generally, errors produced by the latter effect are much smaller (<1%).

b. *Parameterizations of nongray gaseous absorption*

In each band shown in Table 2, the scattering properties, solar irradiance, and Planck functions may be treated as constant. In the solar spectrum, absorption due to H_2O (2500–14 500 cm^{-1}), O_3 (in the ultraviolet and visible), CO_2 (2850–5250 cm^{-1}), and O_2 (A, B, and γ bands) is accounted for in the parameterization. In the infrared spectrum, we include the major absorption bands of H_2O (0–2200 cm^{-1}), CO_2 (540–800 cm^{-1}), O_3 (980–1100 cm^{-1}), CH_4 (1100–1400 cm^{-1}), and N_2O (1100–1400 cm^{-1}). The continuum absorption of H_2O is incorporated in the spectral region 280–1250 cm^{-1}.

Nongray gaseous absorption is incorporated into the δ-four-stream scheme based on the correlated k-distribution method developed by Fu and Liou (1992). In this method, the cumulative probability, g, of the absorption coefficient, k_ν, in a spectral interval $\Delta\nu$ is used to replace frequency, ν, as an independent variable. This leads to an immense numerical simplification, in which about 10 000 frequency intervals can be replaced by a few g intervals. With the required accuracy of ~1%, we find that the minimum number of quadrature points in the g space ranges from one to about ten for different absorbing gases in different spectral regions. In order to treat overlapping of CO_2 and H_2O absorption, the correlated k distribution has been formulated for a single gas mixture to economize the computational time. Using a minimum number of g intervals to represent the gaseous absorption and to treat overlap within each spectral interval, 121 spectral calculations are required for each vertical profile.

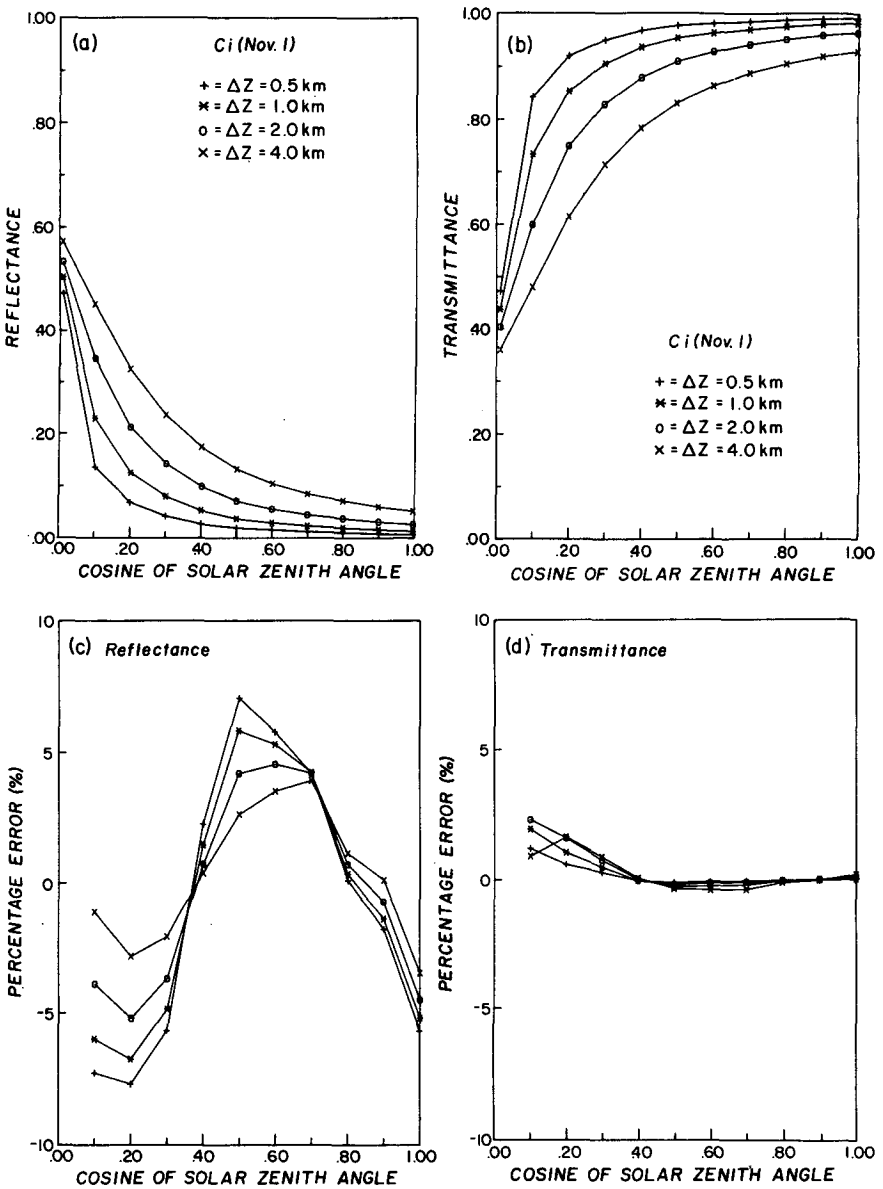

FIG. 3. (a) Solar reflectance and (b) solar transmittance calculated by the adding method using "exact" phase function for Ci (1 Nov). The corresponding percentage errors in solar reflectance and transmittance produced by the δ-four-stream scheme with parameterizations of the single-scattering properties are displayed in (c) and (d).

In the correlated k-distribution method, the vertical nonhomogeneity of the atmosphere is accounted for by assuming a simple correlation of k distribution at different temperatures and pressures. The accuracy of the δ-four-stream scheme coupled with the parameterization program for nongray gaseous absorption has been examined with respect to results computed from a line-by-line program. Shown in Fig. 4a is a comparison of IR cooling rates using the midlatitude summer profile when all the constituents are included in the calculations. A maximum heating rate difference of 0.08 K day^{-1} occurs in the troposphere. The errors in the calculated flux are within 0.3%. Figure 4b shows a comparison of solar heating rates due to water vapor for different solar zenith angles. The errors in heating rates are less than 0.05 K day^{-1}. The errors in total atmospheric absorption and downward surface fluxes are generally less than 0.5%.

c. *Molecular scattering*

The average extinction coefficient due to molecular scattering for a given band may be expressed as (Slingo and Schrecker 1982)

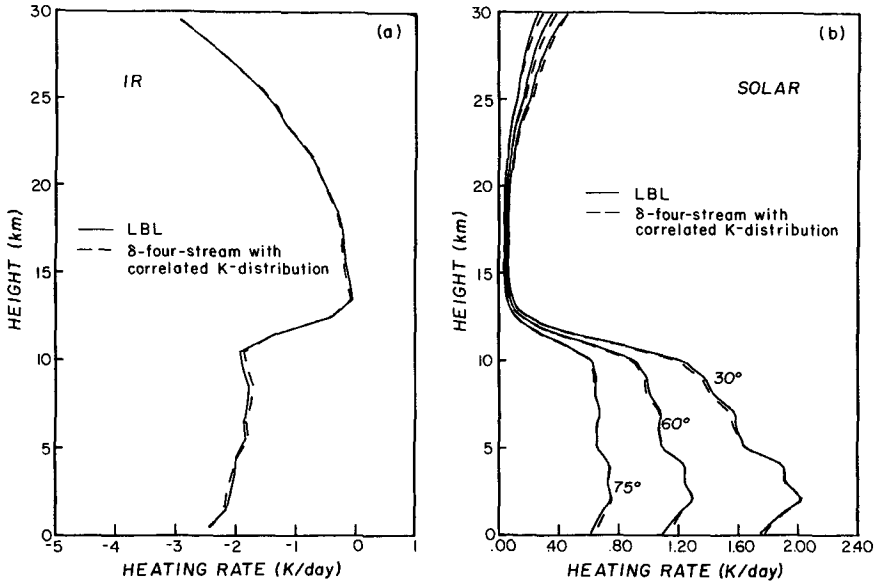

FIG. 4. Comparisons between the present model and line-by-line calculations for (a) infrared cooling rates due to H_2O (with continuum) + CO_2 + O_3 + CH_4 + N_2O in the spectral region 1–2200 cm^{-1}, and (b) solar heating rates due to H_2O in the spectral region 2500–14 500 cm^{-1}, in the midlatitude summer atmosphere.

$$\beta = Rp/T, \tag{3.2}$$

where p is pressure (mb), T is temperature (K), and β is in units of inverse meter. The coefficients R for the six bands in the solar spectrum are 9.022×10^{-6}, 5.282×10^{-7}, 5.722×10^{-8}, 1.433×10^{-8}, 4.526×10^{-9}, and 1.529×10^{-9}.

For Rayleigh scattering, the single-scattering albedo is 1. The phase function $P(\cos\theta) = \frac{3}{4}(1 + \cos^2\theta)$, so that the expansion coefficients $\tilde{\omega}_1 = 0$, $\tilde{\omega}_2 = 1/2$, and $\tilde{\omega}_l = 0$, where $l \geq 3$.

d. *Single-scattering properties for combined cloud particles and gases*

Consider a nonhomogeneous atmosphere that is divided into N homogeneous layers. For the case when both Rayleigh scattering and extinction by cloud particles are mixed with gaseous absorption, the total optical depth for each layer is

$$\Delta\tau(g) = \Delta\tau^{R} + \Delta\tau^{M} + \Delta\tau^{G}(g), \tag{3.3}$$

where $\Delta\tau^{R}$ and $\Delta\tau^{M}$ represent the optical depth due to Rayleigh molecules and cloud particles, respectively; $\Delta\tau^{G}(g)$ is the optical depth contributed by the gaseous absorption for a given g (the cumulative probability), which can be expressed by

$$\Delta\tau^{G}(g) = k(g, p, T)\rho\Delta z, \tag{3.4}$$

where $k(g, p, T)$ is the equivalent k function (Fu and Liou 1992), ρ is the density of the absorber, and Δz is the geometric thickness of the layer. In this case, $\Delta\tau^{M} = \Delta\tau_s^{M} + \Delta\tau_a^{M}$, where $\Delta\tau_s^{M}$ and $\Delta\tau_a^{M}$ are cloud scattering and absorption optical depths, respectively. Thus, the combined single-scattering albedo and the expansion coefficients for the phase function can be obtained by

$$\tilde{\omega}(g) = \frac{\Delta\tau^{R} + \Delta\tau_s^{M}}{\Delta\tau^{R} + \Delta\tau^{M} + \Delta\tau^{G}(g)}, \tag{3.5}$$

$$\tilde{\omega}_l = \frac{\Delta\tau_s^{M}\tilde{\omega}_l^{M} + \Delta\tau^{R}\tilde{\omega}_l^{R}}{\Delta\tau_s^{M} + \Delta\tau^{R}}, \tag{3.6}$$

where $\tilde{\omega}_l^{M}$ and $\tilde{\omega}_l^{R}$ denote the expansion coefficients for the phase function for cloud particles and Rayleigh molecules, respectively. Since the phase function is independent of gaseous absorption, the combined $\tilde{\omega}_l$ is constant over a given spectral absorption band. Once the single-scattering properties have been defined for a given g for each level, monochromatic radiative transfer calculations may be carried out, and the total flux over each spectral band can be obtained by integrating the flux solution in the g space. As described in section 3b, a number of intervals are used for the g quadrature, which are sufficient to confine the integration errors within 1%.

4. Comparisons with observations

Recently, the cirrus intensive field observation (IFO) was conducted in Wisconsin from 13 October to 2 November 1986 as a major component of the First ISCCP Regional Experiment (FIRE) to improve our understanding of cirrus clouds and their influence on weather

and climate processes (Starr 1987). In cirrus IFO, the microphysical measurements were simultaneously obtained along with radiation measurements by using high altitude research aircraft. This allows comparisons to be made between model calculations and in situ observations. In this section we present comparisons of model-derived infrared emissivity and solar albedo with those obtained from the National Center for Atmospheric Research (NCAR) Sabreliner on 28 October 1986.

The Sabreliner was flown near the western shore of Lake Michigan in the vicinity of Green Bay, Wisconsin, in a thin banded cirrus layer, between 1530 and 1630 UTC (0930–1030 local time). The cloud top and base heights were about 11.1 and 8.9 km, respectively. A racetrack pattern was flown at six different levels throughout the cirrus. The mean solar zenith angle during the flight was 61.3°. Since radiative and microphysical characteristics of the cloud sampled on the south side of the racetrack (referred to as cloud 1) are different from those sampled on the north side (referred to as cloud 2), the data from each side were analyzed separately. Furthermore, each side of the racetrack pattern was divided into thinner, mean, and thicker cases to minimize the sampling error. Details of the description of the observations and data analysis procedure have been given by Smith et al. (1990) and Heymsfield et al. (1990).

The effective upward emissivity $\epsilon^{\uparrow}$ and downward emissivity $\epsilon^{\downarrow}$ involving a nonblack cloud may be defined as (Paltridge and Platt 1981)

$$\epsilon^{\uparrow} = \frac{F_L^{\uparrow}(z_t) - F_L^{\uparrow}(z_b)}{\sigma \bar{T}^4 - F_L^{\uparrow}(z_b)}, \tag{4.1}$$

and

$$\epsilon^{\downarrow} = \frac{F_L^{\downarrow}(z_b) - F_L^{\downarrow}(z_t)}{\sigma \bar{T}^4 - F_L^{\downarrow}(z_t)}, \tag{4.2}$$

where $F_L^{\uparrow}$ and $F_L^{\downarrow}$ are the infrared broadband upward and downward fluxes, z_t and z_b are the cloud top and base heights, and $\bar{T}$ is the mean cloud temperature; $\sigma \bar{T}^4$ is the flux emitted by a blackbody at $\bar{T}$.

The solar albedo may be defined as (Paltridge and Platt 1981)

$$\alpha = \frac{F_S^{\downarrow}(z_t)(1-a) - F_S^{\downarrow}(z_b)}{F_S^{\downarrow}(z_t) - F_S^{\uparrow}(z_b)}, \tag{4.3}$$

where

$$a = \frac{[F_S^{\downarrow}(z_t) - F_S^{\uparrow}(z_t)] - [F_S^{\downarrow}(z_b) - F_S^{\uparrow}(z_b)]}{F_S^{\downarrow}(z_t) + F_S^{\uparrow}(z_b)}. \tag{4.4}$$

In these equations, F_S is the solar broadband flux.

Here $\epsilon^{\uparrow}$, $\epsilon^{\downarrow}$, and α were derived from broadband flux observations by Stackhouse and Stephens (1991) for the 28 October 1986 FIRE case, which are shown in Figs. 5a–c as a function of the ice water path (IWP), defined as IWC · Δz. The error bars through these observation points denote the uncertainties of the observation. The theoretical results are displayed in these figures for comparisons. In the calculations, atmospheric temperature and moisture profiles were averaged over the two soundings from Green Bay at 1400 and 1730 UTC. For CO_2, CH_4, and N_2O, uniform mixings were assumed throughout the atmosphere with concentrations of 330, 1.6, and 0.28 ppmv, respectively. The ozone profile and the temperature and moisture profiles above sounding were assumed to be those of the *U.S. Standard Atmosphere*. The cloud was positioned between 8.9 and 11.1 km and the IWP was varied by changing the assumed IWC but keeping the cloud position fixed. Ice saturation mixing ratio was assumed in the cloud. In the computations, the mean effective sizes of 25, 50, 75, 100, and 125 μm were used, corresponding to five solid lines for $\epsilon^{\uparrow}$, $\epsilon^{\downarrow}$, and α in Figs. 5a–c. For solar radiation, the solar zenith angle used was 61.3° and surface albedo was assumed to be 0.072 (Stackhouse and Stephens 1991). Comparing the theoretical results to observed data, we find that the mean effective sizes of these cases lie in the range of ~50–~100 μm for $\epsilon^{\uparrow}$ and $\epsilon^{\downarrow}$, and ~50–~75 μm for α. The mean effective size for $\epsilon^{\uparrow}$ and $\epsilon^{\downarrow}$ in each case appears to be consistent in view of the observational uncertainties; however, the mean effective size associated with solar albedo is smaller than that associated with effective emissivity. This difference can be explained by the fact that solar albedo is more sensitive to the size spectra at the cloud top. Based on observations (Heymsfield et al. 1990), ice crystals progressively range from smaller sizes near the cloud top to larger sizes at the base of the cloud. For the same cloud, for example, cloud 1, Fig. 5 shows that D_e increases as IWP increases. This is expected because larger IWC is usually correlated with larger particle size. As given by Eqs. (4.1) and (4.2), the effective emissivities are defined in terms of fluxes that contain components due to scattering of cloud particles and absorption of gases, principally water vapor. For this reason, the computed effective emissivities may exceed 1 when IWP is large, and may deviate from 0 when IWP → 0. Figure 5d illustrates the plot of solar albedo versus effective downward emissivity for a number of mean effective sizes. The observed data derived from the 28 October 1986 FIRE case are also displayed. In the domain of albedo–emissivity, the effect of ice crystal size distribution is fairly small. Reasonable agreements are shown between the theoretical results and observations.

We also calculate the emissivity of cloud particles alone by using the δ-four-stream scheme with the parameterized single-scattering properties described in section 2. The results are compared with those derived by Smith et al. (1990) for the 28 October 1986 FIRE case in Fig. 6, where each pair of observed points represents the emittance from the top layer of the cloud and the emittance of the entire cloud layer. Smith et

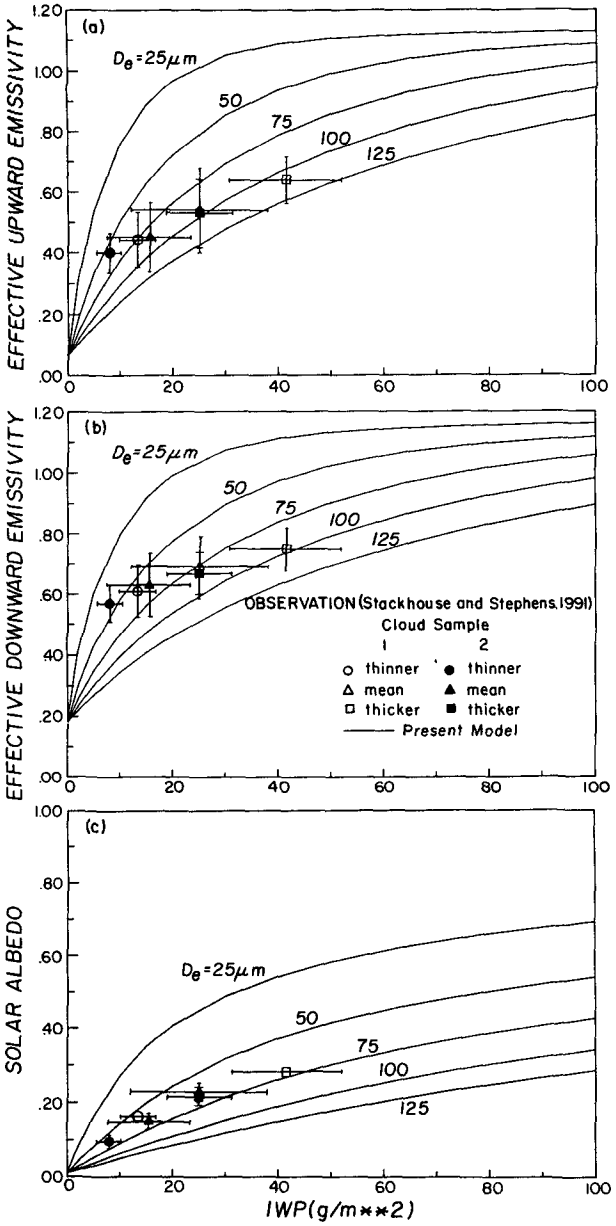

FIG. 5. (a) Effective upward emissivity, (b) effective downward emissivity, and (c) solar albedo as functions of the ice water path. Model results representing the mean effective sizes of 25, 50, 75, 100, and 125 μm are compared with the observed values obtained from the cirrus FIRE IFO.

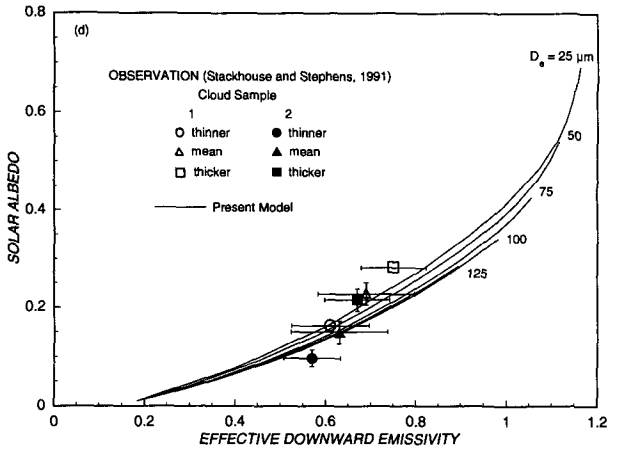

FIG. 5. (*Continued*) (d) Solar albedo as a function of effective downward emissivity. Model results for the mean effective sizes of 25, 50, 75, 100, and 125 μm are compared with the observed values obtained from the cirrus FIRE IFO.

al. utilized a broadband infrared radiative transfer model (Cox and Griffith 1979) to isolate the emissivity of ice particles by using observed downward infrared fluxes. From this comparison (Fig. 6), we find that the average D_e of the entire cloud layer is in agreement with the value derived from Fig. 5a for each case. Figure 6 also shows that the averaged mean effective size in the upper layer of the cloud is generally smaller than that of the entire cloud layer. From Fig. 6, we note that the line for the D_e of 25 μm crosses the 50-μm line. This is because a smaller D_e produces larger reflectivity, r. When the optical depth $\tau \to \infty$, the emissivity $\epsilon = 1 - r$ would be smaller.

From Figs. 5 and 6, the estimated D_e ranges from ~50 to ~100 μm. Using aspect ratios of 2 for 50 μm and 3 for 100 μm, the effective maximum dimension (L_e) would be from ~100 to ~300 μm. Wielicki et al. (1990) estimated the median mass weighted maximum dimension (L_m) from Sabreliner observations to be ~75 to ~400 μm. The averaged L_m is ~238 μm. The averaged L_e from the present study is ~200 μm. Note that L_m and L_e represent volume and area-weighted mean values. Nevertheless, the computed L_e from the model appears to compare reasonably well with observed data.

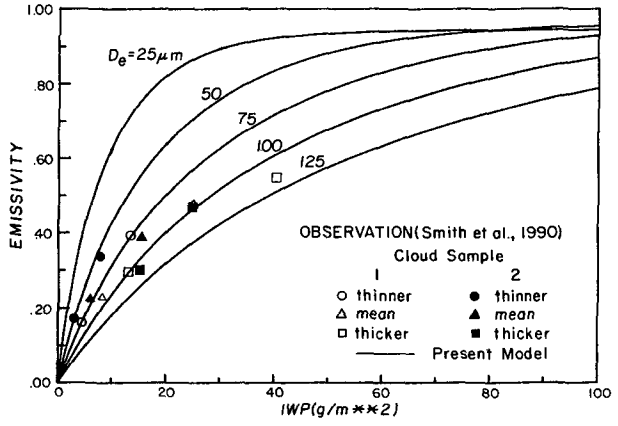

FIG. 6. The emissivity of cloud particles alone as a function of the ice water path. Model results for the mean effective sizes of 25, 50, 75, 100, and 125 μm are compared with the observed values obtained from the cirrus FIRE IFO.

In light of preceding discussion, the observed cloud emissivity and cloud albedo can be reasonably interpreted from the theoretical results, which used the scattering and absorption properties for hexagonal ice crystals (columns and plates). The actual ice crystals that were collected by the optical probe aboard the Sabreliner during the FIRE cirrus experiment were largely bullet rosettes, columns, plates, and compacted spatial particles (occasionally having extensions) (Heymsfield et al. 1990). Although the exact ice crystal shapes were not employed in the scattering and absorption calculations, the theoretical results account for the general hexagonal structure of ice particles and include accurate flux calculations. This perhaps explains some success of the present parameterization scheme in the interpretation of the observed data from aircraft. Past researchers frequently used area-equivalent spheres to interpret the observed radiative properties of cirrus (see, e.g., Stackhouse and Stephens 1991). Since equivalent spheres scatter more light in forward directions and have smaller single-scattering albedo than nonspherical ice crystals, the assumption that ice particles are spheres would lead to an underestimation of the solar albedo of cirrus clouds (Kinne and Liou 1989). Increasing the amount of small spherical ice crystals has not led to a better interpretation of the radiative properties of cirrus clouds. Finally, it should be pointed out that further verification of theoretical results would require narrowing the large experimental uncertainties that are related to radiation and microphysical measurements.

Finally, we examine the relationship for the emissivity of cirrus clouds as a function of the optical depth at 0.55 μm. Using the present model, a number of emissivities were computed for the 11 observed cirrus cloud types (Table 1) with cloud thicknesses of 0.5, 1, 2, and 4 km. The results are plotted in Fig. 7 as a function of the optical depth. The solid line on the diagram is the least square curve using the function

$$\epsilon = 1 - \exp(-a\tau), \qquad (4.5)$$

where τ is the visible optical depth. The fitted coefficient a is 0.79. Using a diffusivity factor of 1.66, the visible optical depth is related to the infrared optical depth (due to absorption) by a factor of 2.1. This result agrees with the observed result reported by Platt et al. (1987), who showed that the ratio of visible extinction to infrared absorption varies from ~1.8 to 2.3 for the midlatitude cirrus clouds. Note that the 11 size distributions used in the present study cover a spectrum of ice crystal size spectra that occur in midlatitude cirrus clouds.

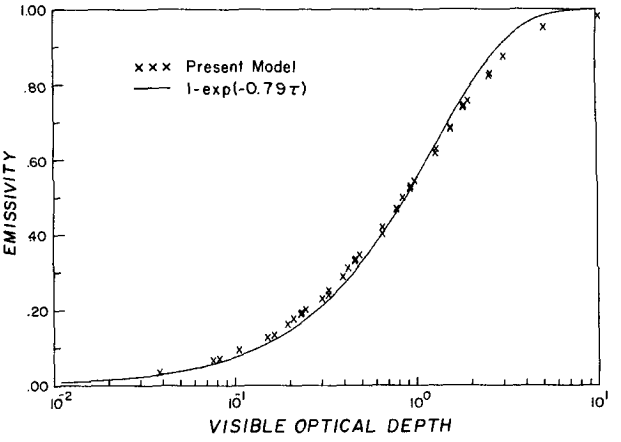

FIG. 7. The emissivity of cirrus clouds as a function of the visible optical depth. The "x" points are obtained from the present model for the 11 cloud types (Table 1) with thicknesses of 0.5, 1, 2, and 4 km. The solid line is from least-square fits.

5. The radiative effects of ice crystal size distributions

The importance of cirrus clouds on the radiative budget of the earth and the atmosphere has been documented by Liou (1986). Ackerman et al. (1988) have further carried out an investigation regarding the interaction of infrared and solar radiation with tropical cirrus anvils. They find that the radiative effects of cirrus clouds are very sensitive to the assumed ice water content, the cloud thickness, and the environmental conditions in which the clouds form. Their study, however, was confined to cirrus clouds with a fixed size distribution. In this study, we examine the effects of ice crystal size distributions on the radiative heating and budget using the radiative transfer model developed in the preceding sections. In the present calculations, standard atmospheric temperature, water vapor, and ozone profiles are used. The cirrus cloud layer is inserted in the atmosphere between 9 and 11 km. For water vapor within the cloud layer, the ice saturation mixing ratio is assumed. To compute solar fluxes, a solar constant of 1365 W m^{-2}, a surface albedo of 0.1, a solar zenith angle of 60°, and a 12-h solar day are used. The computations are carried out by using the mean effective sizes, D_e, of 25, 50, 75, 100, and 125 μm, which cover the range of D_e from observations.

a. Heating rate

The effects of the ice crystal mean effective size on IR, solar, and net (IR + solar) radiative heating rates in the cloud are illustrated in Figs. 8a, 8b, and 8c, respectively. The IWP used is 30 g m^{-2}, which corresponds to an IWC of 0.015 g m^{-3}. In the calculations, the vertical layer thickness is set to be 250 m and the heating rates are layer averages. For the smallest D_e (25 μm), IR heating/cooling rates of about 30 K day^{-1} take place close to the bottom and top of the cloud layer. Such large differential heating rates between cloud bottom and top (~60 K day^{-1}) would have a significant effect on both the entrainment and cloud microphysics (Ackerman et al. 1988). For the largest

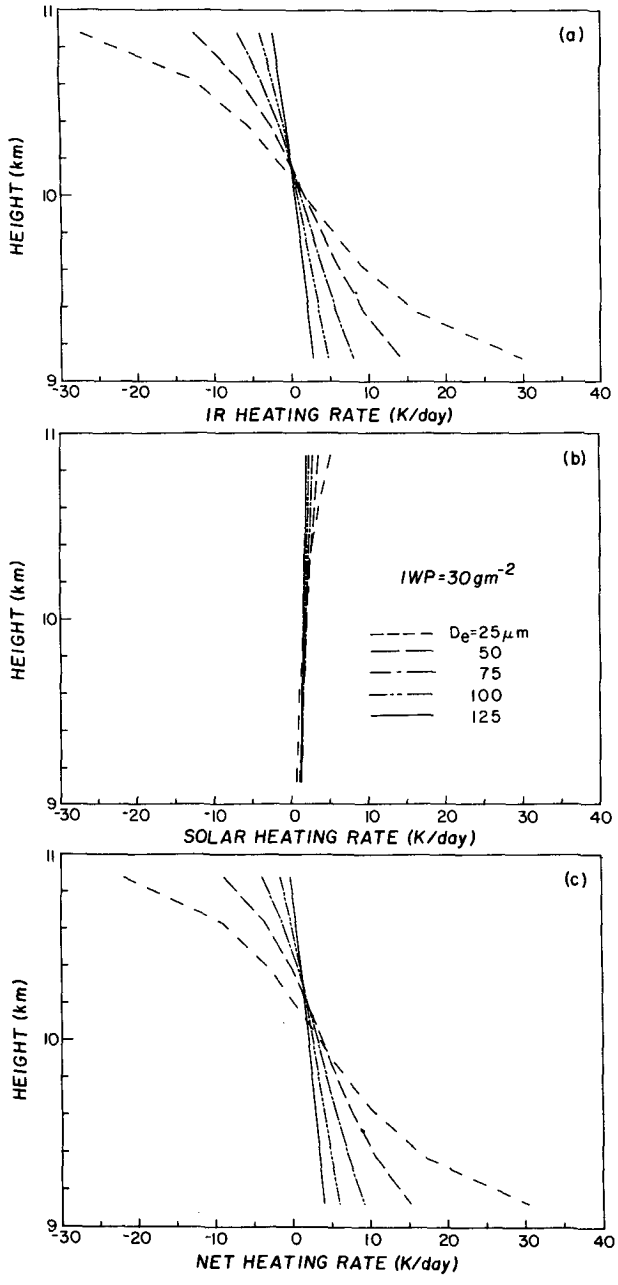

FIG. 8. Heating rates in a cirrus cloud with an ice water content of 0.015 g m^{-3} for five mean effective sizes of 25 (short dash), 50 (long dash), 75 (short-long dash), 100 (double short-long dash), and 125 μm (solid). (a) Infrared, (b) solar, and (c) net. For solar radiation, the solar zenith angle is 60°, the surface albedo is 0.1, and a 12-h solar day is used.

D_e of 125 μm, the IR heating/cooling rates at the cloud bottom and top reduce by as much as a factor of 10. A cloud consisting of smaller D_e emits more IR radiation at the cloud top, resulting in strong cooling. The cloud absorbs, at the same time, more IR radiation emitted from the warmer surface and atmosphere below, resulting in strong heating at the cloud-base region. If IWC is fixed, a cloud containing smaller D_e would have larger emittance/absorptance because of larger cross-sectional area. The solar heating rate peaks at the cloud top and reaches a value of ~5 K day^{-1} for D_e of 25 μm. The net heating rates due to both IR and solar radiation in the cloud are shown in Fig. 8c. It is evident that the cloud heating rate field is largely controlled by IR radiation and that smaller D_e can produce larger radiative heating gradients.

For a given ice crystal size distribution, larger IWC generates a stronger radiative heating gradient, as demonstrated by Ackerman et al. (1988). Based on the preceding discussion on the relation of D_e and heating rates, changes in the heating gradient due to the effects of D_e and IWC are thus in opposite directions. According to observations (e.g., Heymsfield et al. 1990), IWC usually (if not always) increases with increasing ice crystal size. Therefore, the effects of IWC and D_e on heating rates may partially be compensated for if both parameters are interactively included in the calculation.

b. *Cloud forcing*

The ice crystal size distribution of cirrus clouds has a significant effect on the radiation budget of the earth and the atmosphere. To quantify this effect, we use the cloud radiative forcing concept (e.g., Hartmann et al. 1986) for the flux at the top of the atmosphere (TOA) and define the following:

$$C_{\mathrm{ir},s} = F^{\mathrm{cl}}_{\mathrm{ir},s} - F^{\mathrm{ov}}_{\mathrm{ir},s},$$

where cl and ov denote clear and overcast conditions, and F_{ir} and F_s are the upward IR and solar fluxes, respectively. The net cloud radiative forcing is

$$C = C_{\mathrm{ir}} + C_s.$$

For partly cloudy conditions, if the cloud cover is denoted as η, the cloud radiative forcing is given by ηC.

Figures 9a–c show the results of C_{ir}, C_s, and C as a function of IWP for different mean effective sizes. The IR cloud forcing C_{ir} (Fig. 9a) is always positive, corresponding to the heating of the earth–atmosphere system due to the greenhouse effect of clouds, while the solar cloud forcing C_s (Fig. 9b) is always negative, showing the cooling of the system by the cloud albedo effect. Terms C_{ir} and C_s are strongly dependent on both IWP and D_e. For an IWP of 30 g m^{-2}, C_{ir} decreases from 131 to 54 W m^{-2} as D_e increases from 25 to 125 μm. The solar cloud forcing counterpart increases from −114 to −24 W m^{-2}. The net cloud forcing (Fig. 9c) shows that cirrus clouds have a net heating effect on the system except for IWP > 50 g m^{-2} in the case when D_e = 25 μm. These results are similar to those derived from a climate model presented by Stephens et al. (1990).

Usually, small D_e is associated with cold cirrus clouds that have small IWP. We may safely assume that mid-

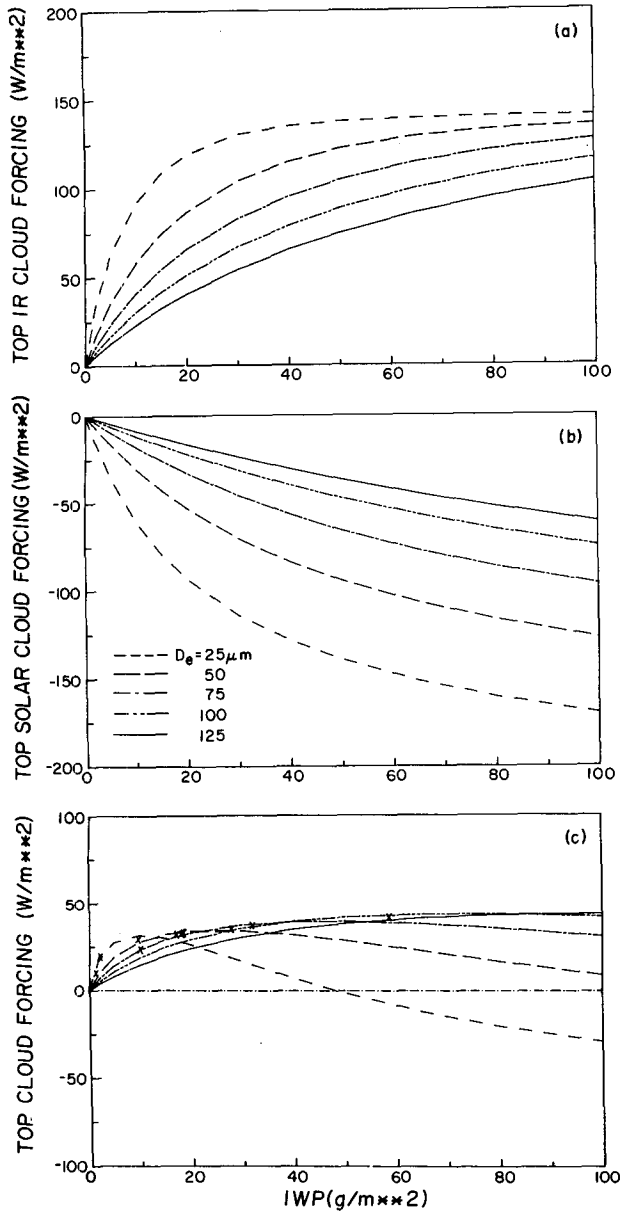

FIG. 9. Cloud radiative forcing at the top of the atmosphere as a function of the ice water path for five mean effective sizes of 25 (short dash), 50 (long dash), 75 (short-long dash), 100 (double short-long dash), and 125 μm (solid). (a) Infrared, (b) solar, and (c) net. For solar radiation, the solar zenith angle is 60°, the surface albedo is 0.1, and a 12-h solar day is used.

latitude cirrus clouds would have positive cloud forcing; that is, the greenhouse effect produced by the presence of these clouds is more pronounced than the albedo effect. The net greenhouse effect is a function of both ice crystal size and IWP. The data points depicted in Fig. 9c are computed from the ten observed ice crystal size distributions (except Ci uncinus, which has a IWP of $\sim$220 g m^{-2}) using a thickness of 2 km. The visible optical depths of these clouds range from about 0.15 to 1.5. Assuming a 20% cloud cover, the cloud forcing values generally range from about 4 to 8 W m^{-2}. When coupled with positive radiative forcings, such as those due to the increase of greenhouse gases, feedbacks produced by the increase or decrease of cirrus parameters could be significant.

Finally, we investigate the cloud radiative forcing at the surface. Figures 10a and 10b show the IR and solar cloud forcing, respectively. In the latter case, the negative cloud forcing values produced by cloud reflection are substantially similar to those presented in Fig. 9b. This is because the atmosphere is largely transparent with respect to solar radiation when clouds are present. For the IR case, the insertion of cirrus clouds produces small effects at the surface (0–30 W m^{-2}), because of the strong absorption of the atmosphere between the surface and the cloud in the infrared wavelengths. The cirrus cloud–induced IR heating within the atmosphere and solar cooling at the surface could have a significant impact on the atmospheric circulations and temperature distributions (Ramanathan 1987; Slingo and Slingo 1988).

6. Summary and conclusions

In this paper, a new approach has been devised for the parameterization of radiative transfer in the at-

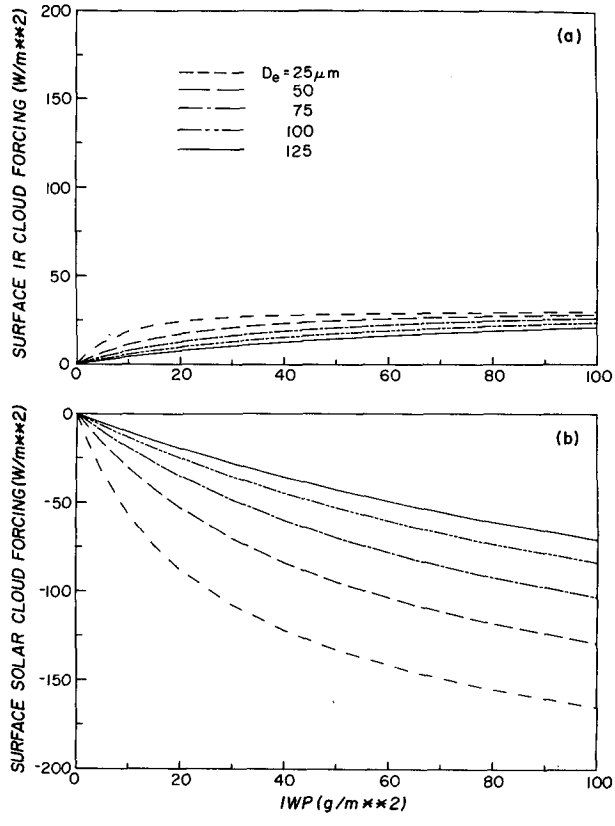

FIG. 10. Same as Fig. 9 except for the cloud radiative forcing at the surface. (a) Infrared and (b) solar.

mosphere involving cirrus clouds. We use a mean effective size, representing ice crystal size distribution, in the development of parameterization for the single-scattering properties of ice crystals. The extinction coefficient, the single-scattering albedo, and the expansion coefficients of the phase function for the 11 observed ice crystal size distributions have been computed from a geometric ray-tracing technique for hexagonal ice crystals (size parameter > 30) and Mie-type solution for spheroids (size parameter < 30). Using these results and basic physical reasonings, we develop simple polynomial relationships between the single-scattering properties and mean effective size that can achieve relative accuracies within ~1%.

A δ-four-stream radiative transfer scheme has been developed for flux calculations in both solar and infrared spectra. With respect to the "exact" results computed from the adding method for radiative transfer, this scheme can yield relative accuracies within ~5% for all atmospheric conditions. For nongray gaseous absorptions due to H_2O, CO_2, O_3, CH_4, and N_2O, we use the correlated k-distribution method to obtain a number of equivalent absorption coefficients. A total of 121 spectral calculations for each vertical profile in the entire spectrum is required. Compared with line-by-line calculations for clear midlatitude summer atmosphere, the δ-four-stream scheme coupled with the correlated k-distribution parameterization produces deviations less than 0.1 K day^{-1} in heating rates and within 0.5% in flux calculations. In the limit of no scattering, the δ-four-stream scheme can produce reliable results since the double Gauss quadrature provides a correct relation between the flux and intensity from an isotropic source. The computational time of the scheme is linear with respect to the number of vertical levels.

Comparisons have been carried out between theoretical calculations and aircraft measurements involving cloud emissivity and cloud albedo obtained during the cirrus FIRE IFO. The effect of ice crystal size distribution in terms of the mean effective size is important in the interpretation of the observed data. Further verification of the model results requires the reduction of large experimental uncertainties in both radiation and microphysical measurements.

We further investigate the effects of ice crystal size distributions on the radiative properties of the atmosphere involving cirrus clouds. For a given ice water path, cirrus clouds containing smaller mean effective sizes reflect more solar radiation, trap more thermal infrared, and produce strong cloud-top cooling and cloud-base heating. This pattern would enhance the in-cloud heating rate gradient, which could be significant in terms of cloud microphysical processes. For the observed midlatitude cirrus cases, the IR greenhouse effect outweighs the solar albedo effect. The degree of the greenhouse effect involving cirrus clouds is a function of cloud cover as well as the mean effective size and liquid water path. Assuming the presence within a sky field of 20% cirrus clouds, a gain of ~4–8 W m^{-2} is obtained from the present calculation. With respect to the surface, the presence of cirrus clouds reduces the solar flux available to the surface. In this case, the solar albedo effect dominates the IR greenhouse effect, which is confined largely within the atmosphere.

There are a number of significant new features in the present radiative scheme. First, the ice crystal size distribution consisting of nonspherical particles is effectively accounted for in the parameterization of the single-scattering properties of cirrus clouds. This is especially important in the determination of the solar albedo of cirrus clouds. Second, the IR and solar radiation regions have been treated in a self-consistent fashion using the same parameterization scheme, which is essential to the investigation of the solar albedo versus IR greenhouse effects involving clouds. Third, the present model can efficiently compute the detailed vertical structure of the heating rate profile within clouds, which is critical to the understanding of the effects of radiation on cloud formation. The present parameterization for the radiative transfer in the atmosphere involving cirrus clouds is well suited for incorporation in numerical models to study the climatic effects of cirrus clouds, as well as to investigate interactions and feedbacks between cloud microphysics and radiation.

Acknowledgments. The research work contained herein has been supported by AFOSR Grant 91-0039, NASA Grant NAG5-1050, and NSF Grant 90-24217. We thank Dr. Y. Takano for providing the single-scattering data that are used in the parameterization.

APPENDIX

The δ-Four-Stream Approximation for a Homogeneous Layer

In the following, we present the necessary equations for the flux calculation using the δ-four-stream approximation. The notations used in Liou et al. (1988) are followed. Let the total optical depth of a layer be τ_1. The upward and downward fluxes at a given optical depth τ ($0 \leq \tau \leq \tau_1$) are given by

$$F^+(\tau) = 2\pi(a_1\mu_1 I_1 + a_2\mu_2 I_2), \quad \text{(A.1)}$$

$$F^-(\tau) = 2\pi(a_1\mu_1 I_{-1} + a_2\mu_2 I_{-2}) + \mu_0\pi F_\odot e^{-\tau/\mu_0}, \quad \text{(A.2)}$$

where the double Gauss quadratures and weights in the four-stream approximation are $\mu_1 = -\mu_{-1} = 0.2113248$, $\mu_2 = -\mu_{-2} = 0.7886752$, and $a_1 = a_{-1} = a_2 = a_{-2} = 0.5$; μ_0 is the cosine of the solar zenith angle; and $\pi F_\odot$ denotes the direct solar flux at the top of the atmosphere ($\pi F_\odot = 0$ in the thermal infrared). The intensity solutions can be written in the form

$$\begin{bmatrix} I_2 \\ I_1 \\ I_{-1} \\ I_{-2} \end{bmatrix} = \begin{bmatrix} \phi_2^+ e2 & \phi_1^+ e1 & \phi_1^- e3 & \phi_2^- e4 \\ \Phi_2^+ e2 & \Phi_1^+ e1 & \Phi_1^- e3 & \Phi_2^- e4 \\ \Phi_2^- e2 & \Phi_1^- e1 & \Phi_1^+ e3 & \Phi_2^+ e4 \\ \phi_2^- e2 & \phi_1^- e1 & \phi_1^+ e3 & \phi_2^+ e4 \end{bmatrix} \begin{bmatrix} G_2 \\ G_1 \\ G_{-1} \\ G_{-2} \end{bmatrix} + \begin{bmatrix} z_2^+ \\ z_1^+ \\ z_1^- \\ z_2^- \end{bmatrix} e^{-f_0\tau}, \quad \text{(A.3)}$$

where $f_0(\text{solar}) = 1/\mu_0$, $f_0(\text{thermal}) = -1/\tau_1 \ln(B_1/B_0)$, B_0 and B_1 are Planck functions evaluated at the top and bottom of the layer, respectively, and the other terms except $G_{\pm 1,2}$ are defined as follows:

$$e1 = e^{-k_1\tau}, \quad e2 = e^{-k_2\tau},$$

$$e3 = e^{-k_1(\tau_1-\tau)}, \quad e4 = e^{-k_2(\tau_1-\tau)},$$

$$z_{1,2}^{\pm} = \frac{1}{2}(\eta_{1,2} \pm \eta'_{1,2}),$$

$$\phi_{1,2}^{\pm} = \frac{1}{2}\left(1 \pm \frac{b_{11}^- - A_{1,2}b_{21}^-}{a^-} k_{1,2}\right),$$

$$\Phi_{1,2}^{\pm} = \frac{1}{2}\left(A_{1,2} \pm \frac{A_{1,2}b_{22}^- - b_{12}^-}{a^-} k_{1,2}\right),$$

where $k_{1,2}$, $A_{1,2}$, $\eta_{1,2}$, $\eta'_{1,2}$, b_{11}^-, b_{21}^-, b_{22}^-, b_{12}^-, and a^- are calculated from the following equations, which are in the order of calculation. The single-scattering albedo is denoted by $\tilde{\omega}$, and $\tilde{\omega}_l$ ($l = 0, 1, 2, 3$) is the expansion coefficient of phase function ($\tilde{\omega}_0 = 1$):

$$b_i(\text{solar}) = \frac{\tilde{\omega}}{4\pi} \pi F_0 \sum_{l=0}^{3} \tilde{\omega}_l P_l(\mu_i) P_l(-\mu_0)/\mu_i$$

$$b_i(\text{thermal}) = (1 - \tilde{\omega})B_0/\mu_i, \quad i = -2, -1, 1, 2,$$

$$c_{i,j} = \frac{\tilde{\omega}}{2} a_j \sum_{l=0}^{3} \tilde{\omega}_l P_l(\mu_i) P_l(\mu_j), \quad i, j = -2, -1, 1, 2$$

$$b_{i,j} = \begin{cases} c_{i,j}/\mu_i, & i \neq j \\ (c_{i,j} - 1)/\mu_i, & i = j, \end{cases}$$

$$b_{22}^{\pm} = b_{2,2} \pm b_{2,-2}, \quad b_{21}^{\pm} = b_{2,1} \pm b_{2,-1}$$

$$b_{12}^{\pm} = b_{1,2} \pm b_{1,-2}, \quad b_{11}^{\pm} = b_{1,1} \pm b_{1,-1}$$

$$b_2^{\pm} = b_2 \pm b_{-2}, \quad b_1^{\pm} = b_1 \pm b_{-1},$$

$$a_{22} = b_{22}^+ b_{22}^- + b_{12}^+ b_{21}^-, \quad a_{21} = b_{22}^- b_{21}^+ + b_{21}^- b_{11}^+$$

$$a_{12} = b_{12}^- b_{22}^+ + b_{11}^- b_{12}^+, \quad a_{11} = b_{12}^- b_{21}^+ + b_{11}^- b_{11}^+$$

$$d_2 = b_{22}^- b_2^- + b_{21}^- b_1^- + b_2^+ f_0$$

$$d_1 = b_{12}^- b_2^- + b_{11}^- b_1^- + b_1^+ f_0,$$

$$a'_{22} = b_{22}^- b_{22}^+ + b_{12}^- b_{21}^+, \quad a'_{21} = b_{22}^+ b_{21}^- + b_{21}^+ b_{11}^-$$

$$a'_{12} = b_{12}^+ b_{22}^- + b_{11}^+ b_{12}^-, \quad a'_{11} = b_{12}^+ b_{21}^- + b_{11}^+ b_{11}^-$$

$$d'_2 = b_{22}^+ b_2^+ + b_{21}^+ b_1^+ + b_2^- f_0$$

$$d'_1 = b_{12}^+ b_2^+ + b_{11}^+ b_1^+ + b_1^- f_0,$$

$$b = a_{22} + a_{11}, \quad c = a_{21}a_{12} - a_{11}a_{22}$$

$$a^- = b_{22}^- b_{11}^- - b_{12}^- b_{21}^-,$$

$$k_1 = [(b + \sqrt{b^2 + 4c})/2]^{1/2}$$

$$k_2 = [(b - \sqrt{b^2 + 4c})/2]^{1/2},$$

$$A_{1,2} = (k_{1,2}^2 - a_{22})/a_{21},$$

$$\eta_1 = (d_1 f_0^2 + a_{12}d_2 - a_{22}d_1)/f'$$

$$\eta_2 = (d_2 f_0^2 + a_{21}d_1 - a_{11}d_2)/f'$$

$$\eta'_1 = (d'_1 f_0^2 + a'_{12}d'_2 - a'_{22}d'_1)/f'$$

$$\eta'_2 = (d'_2 f_0^2 + a'_{21}d'_1 - a'_{11}d'_2)/f'$$

$$f' = f_0^4 - b f_0^2 - c.$$

The coefficients G_i ($i = \pm 1, 2$) are to be determined from radiation boundary conditions. Consider a homogeneous cloud layer characterized by an optical depth τ_1 and assume that there is no diffuse radiation from the top and bottom of this layer; then the boundary conditions are

$$\left.\begin{aligned} I_{-1,-2}(\tau = 0) &= 0 \\ I_{1,2}(\tau = \tau_1) &= 0 \end{aligned}\right\}. \quad \text{(A.4)}$$

The boundary conditions can be modified to include the nonzero diffuse radiation; G_i can be obtained by an inversion of a four-by-four matrix in Eq. (A.3). We note that the only difference in the four-stream formulation between infrared and solar wavelengths is the definition of f_0 and b_i ($i = \pm 1, 2$).

It is possible to incorporate a δ-function adjustment to account for the forward diffraction peak in the context of the four-stream approximation. We may use the similarity principle for radiative transfer to adjust the optical depth, single-scattering albedo, and expansion coefficients of the phase function in the forms (Liou et al. 1988)

$$\tau' = \tau(1 - f\tilde{\omega})$$

$$\tilde{\omega}' = (1 - f)\tilde{\omega}/(1 - f\tilde{\omega})$$

$$\tilde{\omega}'_l = [\tilde{\omega}_l - f(2l + 1)]/(1 - f), \quad l = 1, 2, 3, \quad \text{(A.5)}$$

where the fraction of scattered energy residing in the forward peak, $f = \tilde{\omega}_4/9$.

REFERENCES

Ackerman, T. P., K.-N. Liou, F. P. J. Valero, and L. Pfister, 1988: Heating rates in tropical anvils. *J. Atmos. Sci.*, **45**, 1606–1623.

Asano, S., and M. Sato, 1980: Light scattering by randomly oriented spheroidal particles. *Appl. Opt.*, **19**, 962–974.

Auer, A. H., Jr., and D. L. Veal, 1970: The dimension of ice crystals in natural clouds. *J. Atmos. Sci.*, **27**, 919–926.

Cox, S. K., and K. T. Griffith, 1979: Estimates of radiative divergence during phase III of the GARP Atlantic tropical experiment. Part I: Methodology. *J. Atmos. Sci.*, **36,** 576–585.

Foot, J. S., 1988: Some observations of the optical properties of clouds. II: Cirrus. *Quart. J. Roy. Meteor. Soc.*, **114,** 145–164.

Fu, Q., and K. N. Liou, 1992: On the correlated *k*-distribution method for radiative transfer in nonhomogeneous atmospheres. *J. Atmos. Sci.*, **49,** 2139–2156.

Hansen, J. E., and L. D. Travis, 1974: Light scattering in planetary atmospheres. *Space Sci. Rev.*, **16,** 527–610.

Hartmann, D. L., V. Ramanathan, A. Berroir, and G. E. Hunt, 1986: Earth radiation budget data and climate research. *Rev. Geophys.*, **24,** 439–468.

Heymsfield, A. J., 1975: Cirrus uncinus generating cells and the evolution of cirriform clouds. *J. Atmos. Sci.*, **32,** 799–808.

——, and C. M. R. Platt, 1984: A parameterization of the particle size spectrum of ice clouds in terms of the ambient temperature and the ice water content. *J. Atmos. Sci.*, **41,** 846–855.

——, K. M. Miller, and J. D. Spinhirne, 1990: The 27–28 October 1986 FIRE IFO cirrus case study: Cloud microstructure. *Mon. Wea. Rev.*, **118,** 2313–2328.

Kinne, S., and K. N. Liou, 1989: The effects of the nonsphericity and size distribution of ice crystals on the radiative properties of cirrus clouds. *Atmos. Res.*, **24,** 273–284.

Liou, K. N., 1975: Applications of the discrete-ordinate method for radiative transfer to inhomogeneous aerosol atmospheres. *J. Geophys. Res.*, **80,** 3434–3440.

——, 1986: Influence of cirrus clouds on weather and climate processes: A global perspective. *Mon. Wea. Rev.*, **114,** 1167–1199.

——, 1992: *Radiation and Cloud Processes in the Atmosphere: Theory, Observation, and Modeling.* Oxford University Press, 487 pp.

——, and G. D. Wittman, 1979: Parameterization of the radiative properties of clouds. *J. Atmos. Sci.*, **36,** 1261–1273.

——, Q. Fu, and T. P. Ackerman, 1988: A simple formulation of the δ-four-stream approximation for radiative transfer parameterizations. *J. Atmos. Sci.*, **45,** 1940–1947.

Ono, A., 1969: The shape and riming properties of ice crystals in natural clouds. *J. Atmos. Sci.*, **26,** 138–147.

Paltridge, G. W., and C. M. R. Platt, 1981: Aircraft measurements of solar and infrared radiation and the microphysics of cirrus cloud. *Quart. J. Roy. Meteor. Soc.*, **107,** 367–380.

Platt, C. M. R., and Harshvardhan, 1988: Temperature dependence of cirrus extinction: Implications for climate feedback. *J. Geophys. Res.*, **93,** 11 051–11 058.

——, J. C. Scott, and A. C. Dilley, 1987: Remote sounding of high clouds. Part VI: Optical properties of midlatitude and tropical cirrus. *J. Atmos. Sci.*, **44,** 729–747.

Ramanathan, V., 1987: The role of earth radiation budget studies in climate and general circulation research. *J. Geophys. Res.*, **92,** 4075–4095.

Slingo, A., and H. M. Schrecker, 1982: On the shortwave radiative properties of stratiform water clouds. *Quart. J. Roy. Meteor. Soc.*, **108,** 407–426.

——, and J. M. Slingo, 1988: The response of a general circulation model to cloud longwave radiative forcing. I: Introduction and initial experiments. *Quart. J. Roy. Meteor. Soc.*, **114,** 1027–1062.

Smith, W. L., Jr., P. F. Hein, and S. K. Cox, 1990: The 27–28 October 1986 FIRE IFO cirrus case study: In situ observations of radiation and dynamic properties of a cirrus cloud layer. *Mon. Wea. Rev.*, **118,** 2389–2401.

Stackhouse, P. W., Jr., and G. L. Stephens, 1991: A theoretical and observational study of the radiative properties of cirrus: Results from FIRE 1986. *J. Atmos. Sci.*, **48,** 2044–2059.

Stamnes, K., and P. Conklin, 1984: A new multi-layer discrete ordinate approach to radiative transfer in vertically inhomogeneous atmospheres. *J. Quant. Spectrosc. Radiat. Transfer,* **31,** 273–282.

Starr, D. O., 1987: A cirrus cloud experiment: Intensive field observations planned for FIRE. *Bull. Amer. Meteor. Soc.*, **68,** 119–124.

Stephens, G. L., S. C. Tsay, P. W. Stackhouse, Jr., and P. J. Flatau, 1990: The relevance of the microphysical and radiative properties of cirrus clouds to climate and climate feedback. *J. Atmos. Sci.*, **47,** 1742–1753.

Sykes, J. B., 1951: Approximate integration of the equation of transfer. *Mon. Not. R. Astron. Soc.*, **111,** 377–386.

Takano, Y., and K. N. Liou, 1989: Solar radiative transfer in cirrus clouds. Part I: Single-scattering and optical properties of hexagonal ice crystals. *J. Atmos. Sci.*, **46,** 3–19.

——, ——, and P. Minnis, 1992: The effects of small ice crystals on cirrus infrared radiative properties. *J. Atmos. Sci.*, **49,** 1487–1493.

Thekaekara, M. P., 1973: Solar energy outside the earth's atmosphere. *Sol. Energy,* **14,** 109–127.

Warren, S. G., 1984: Optical constants of ice from ultraviolet to the microwave. *Appl. Opt.*, **23,** 1206–1225.

Wielicki, B. A., J. T. Suttles, A. J. Heymsfield, R. M. Welch, J. D. Spinhirne, M.-L. C. Wu, D. O'C. Starr, L. Parker, and R. F. Arduini, 1990: The 27–28 October 1986 FIRE IFO cirrus case study: Comparison of radiative transfer theory with observations by satellite and aircraft. *Mon. Wea. Rev.*, **118,** 2356–2376.

Wiscombe, W. J., 1976: Extension of the doubling method to inhomogeneous sources. *J. Quant. Spectrosc. Radiat. Transfer,* **16,** 477–489.